Original Article

JCBFM

Journal of Cerebral Blood Flow & Metabolism
2022, Vol. 42(9) 1616–1631

DOI: 10.1177/0271678X221082016
journals.sagepub.com/home/jcbfm

The lateral entorhinal cortex is a hub for local and global dysfunction in early Alzheimer's disease states

Francesca Mandino[1,2,3], Ling Yun Yeow[1], Renzhe Bi[1], Lee Sejin[1], Han Gyu Bae[1,4], Seung Hyun Baek[1], Chun-Yao Lee[1], Hasan Mohammad[1], Corey Horien[3], Chai Lean Teoh[1], Jasinda H Lee[5], Mitchell KP Lai[5], Sangyong Jung[1], Yu Fu[1], Malini Olivo[1], John Gigg[2] and Joanes Grandjean[16]

Abstract

Functional network activity alterations are one of the earliest hallmarks of Alzheimer's disease (AD), detected prior to amyloidosis and tauopathy. Better understanding the neuronal underpinnings of such network alterations could offer mechanistic insight into AD progression. Here, we examined a mouse model (3xTgAD mice) recapitulating this early AD stage. We found resting functional connectivity loss within ventral networks, including the entorhinal cortex, aligning with the spatial distribution of tauopathy reported in humans. Unexpectedly, in contrast to decreased connectivity at rest, 3xTgAD mice show enhanced fMRI signal within several projection areas following optogenetic activation of the entorhinal cortex. We corroborate this finding by demonstrating neuronal facilitation within ventral networks and synaptic hyperexcitability in projection targets. 3xTgAD mice, thus, reveal a dichotomic hypo-connected:resting versus hyper-responsive:active phenotype. This strong homotopy between the areas affected supports the translatability of this pathophysiological model to tau-related, early-AD deficits in humans.

Keywords

fMRI, mouse, Alzheimer's disease, optogenetics, 3xTgAD

Received 9 August 2021; Revised 13 January 2022; Accepted 16 January 2022

Introduction

Tauopathies are a hallmark of many neurodegenerative disorders, including Alzheimer's disease (AD).[1] The leading cause for familial-AD is related to the accumulation of toxic forms of beta-amyloid.[2] In contrast, research into the etiological causes of sporadic-AD, which includes >95% of AD cases,[3] suggests that beta-amyloid is not the main causative agent.[4–6] Clinical trials targeting later stages of AD and focusing on anti-amyloid drugs [7] have mostly failed or, in some cases, made symptoms worse.[8] Moreover, recent work suggests that progressive tau accumulation in the brain may be one of the leading causes of sporadic-AD.[9] In sporadic-AD, accumulation of phosphorylated tau (a precursor of neurofibrillary tangles) can be seen inside neurons, decades before beta-amyloid starts to aggregate.[10] Regions particularly affected by

[1]Singapore Bioimaging Consortium, Agency for Science, Technology and Research, Singapore
[2]Faculty of Biology, Medicine and Health, The University of Manchester, Manchester, UK
[3]Department of Radiology and Bioimaging Sciences, Yale School of Medicine, New Haven, CT, USA
[4]Department of Life Sciences, Yeungnam University, Gyeongsan, South Korea
[5]Department of Pharmacology, Yong Loo Lin School of Medicine, National University of Singapore, Singapore
[6]Department of Radiology and Nuclear Medicine & Donders Institute for Brain, Cognition, and Behaviour, Donders Institute, Radboud University Medical Centre, The Netherlands

Corresponding author:
Joanes Grandjean, Department of Radiology and Nuclear Medicine & Donders Institute for Brain, Cognition, and Behaviour, Donders Institute, Radboud University Medical Centre, Nijmegen 6525 EZ, The Netherlands.
Email: Joanes.Grandjean@radboudumc.nl

tau-accumulation in the initial stages of this pathology include the entorhinal cortices and hippocampal formation.[11] These early pathological signs coincide with changes in functional connectivity measured both at rest and during tasks in groups at risk for AD, that is, prior to the overt accumulation of beta-amyloid forms and neurofibrillary tangles.[12,13]

As such, there is increased interest in identifying predictive biomarkers at the earliest stages of illness, well before symptoms have become clinically apparent. Synaptic dysfunction is one such candidate,[14] and is thought to lead to a discrepancy in resting vs. evoked functional activity patterns in early AD. For example, decreased connectivity patterns are typically observed at rest, while increased connectivity is observed during tasks in patients with early AD.[15–18] However, understanding the pathological mechanisms behind the connectivity changes observed in AD patients is difficult due to the limited access of acute recordings.[19]

Transgenic animals bearing mutations from familial AD and tauopathies also develop several of the distributed network dysfunctions found in AD, such as in the early stages of cerebral amyloidosis.[20–22] To understand the physiological basis underlying discrepant resting vs. evoked brain activity patterns during early-AD, we used the triple-transgenic mouse model for AD (3xTgAD).[23] The 3xTgAD is one of the few models that presents accumulation of both beta-amyloid plaques and neurofibrillary tangles later in life. These mice carry two mutations associated with familial AD, namely APP_{SWE} (for amyloid-precursor protein) and Presenilin-1(M146V), leading to progressive accumulation of beta-amyloid forms in the brain, and one mutation associated with frontotemporal dementia, $TauP_{301L}$, which is linked to aberrant tau protein accumulations.

Here, young (3 months) 3xTgAD mice were already positive for phosphorylated tau (phospho-tau, precursor of neurofibrillary tangles), in the amygdala. Phospho-tau labelling progressed to the hippocampus by 6 months; however, no evidence for soluble/insoluble aberrant beta-amyloid was found at the time points investigated. We then assessed the same time points of 3 and 6 months with functional MRI, first at rest (rsfMRI) and subsequently by optogenetically stimulating the lateral entorhinal cortex (ENTl), a central dysfunctional node in 3xTgAD [24,25] and AD patients.[26–28]

Local connectivity in 3xTgAD was disrupted at rest, resulting in macroscale network dysfunction already by 3 months of age. The spatial distribution of these deficits showed a high degree of overlap with homologous networks affected by tauopathies in humans,[29,30] suggesting that the 3xTgAD mouse, although a model of familial-AD, may share a similar pathological profile with human sporadic-AD. Interestingly, optogenetic stimulation of the ENTl revealed a hyperemic response in 3xTgAD relative to wild-type in several distal projection areas. This was further corroborated by direct evoked potential neuronal recordings *in vivo,* which revealed neuronal hyperexcitability in the amygdala and hippocampal areas.

Our observations underscore several of the physiological underpinnings behind local and distal connectivity dysfunction commonly observed in groups at risk of developing AD and other tauopathies, supporting a reconciliation of the apparent discordant results described in early AD subjects.[12,15,31] This study provides a neurophysiological model of early network disturbances in AD and points to key translational targets of clinical interest.

Material and methods

Animal permit

All procedures conducted in the UK were performed in accordance with the UK Animals (Scientific Procedures) Act 1986 and the University of Manchester Ethical Review Panel under Home Office license PPL 70/7843. All experiments performed in Singapore Bioimaging Consortium, A*STAR, Singapore, were in accordance with the ethical standards of the Institutional Animal Care and Use Committee (A*STAR Biological Resource Centre, Singapore, IACUC #171203). All experiments conducted in this work are reported in compliance with ARRIVE guidelines (Animal Research: Reporting in Vivo Experiments).

The detailed breakdown of animal group sizes per experiment is detailed in Supplementary Table S1. Reported below, details for the fMRI experiments; more complete description for electrophysiological recordings (*in* and *ex vivo*) and histology validation can be found in the Supplementary Methods.

Specifically, male 3xTgAD and control mice on the same background strain (129sv/c57bl6) aged either 3–4 months ($N = 6$ and $N = 7$, respectively) or 6–7 months old ($N = 4$ and $N = 4$, respectively) were used for electrophysiological recordings *in vivo*. Additionally, male controls (total $N = 29$) and 3xTgAD (total $N = 31$) have been used for the imaging experiments. Specifically, $N_{controls} = 10$ and $N_{3xTgAD} = 19$ underwent rsfMRI experiments. Additionally, $N_{controls} = 19$ and $N_{3xTgAD} = 12$ mice underwent ofMRI experiments. An *a priori* power analysis was performed following results in [32] using R (power.t.test), indicating that $N = 10$ per group for rsfMRI is sufficient to achieve 80% power with the following parameters: delta = 14, SD = 11, two-tailed test, significance threshold = 0.05.

Animal preparation for imaging

Animal preparation followed a previously established protocol.[33] Anesthesia was induced with 4% isoflurane; subsequently, the animals were endotracheally intubated, placed on an MRI-compatible cradle, and artificially ventilated (90 breaths/minute; Kent Scientific Corporation, Torrington, Connecticut, USA). A bolus with a mixture of Medetomidine (Dormitor, Elanco, Greenfield, Indiana, USA) and Pancuronium Bromide (muscle relaxant, Sigma-Aldrich Pte Ltd, Singapore) was administered subcutaneously (0.05 mg/kg), followed by a maintenance infusion (0.1 mg/kg/hr) administered 5 minutes later, with isoflurane reduced and kept to 0.5%. Functional MRI was acquired 20 min following maintenance infusion onset to allow for the animal state to stabilize. Care was taken to maintain the temperature of the animals at 37 °C.

Data acquisition and stimulation protocols

Data were acquired on an 11.75 T (Bruker BioSpin MRI, Ettlingen, Germany) equipped with a BGA-S gradient system, a 72 mm linear volume resonator coil for transmission. A 2×2 phased-array cryogenic surface receiver coil was adopted for the rsfMRI experiment (N = 29) and a 10 mm single-loop surface coil for ofMRI experiments (N = 31). Images were acquired using Paravision 6.0.1 software.

For the rsfMRI data acquisition, an anatomical reference scan was acquired using a spin-echo turboRARE sequence: field of view (FOV) = $17 \times 9\,mm^2$, FOV saturation slice masking non-brain regions, number of slices = 28, slice thickness = 0.35, slice gap = 0.05 mm, matrix dimension (MD) = 200×100, repetition time (TR) = 2750 ms, echo time (TE) = 30 ms, RARE factor = 8, number of averages = 2. Functional scans were acquired using a gradient-echo echo-planar imaging (EPI) sequence with the same geometry as the anatomical: MD = 90×60, TR = 1000 ms, TE = 15 ms, flip angle = 50°, volumes = 600, bandwidth = 250 kHz, one scan per session, ~10 mins long.

Parameters for the ofMRI data acquisition were adapted to the lower sensitivity of the room temperature receiver coil. The anatomical reference scan was acquired using FOV = $20 \times 10\,mm^2$, number of slices = 34, slice thickness = 0.35, slice gap = 0 mm, MD = 200×100, TR = 2000 ms, TE = 22.5 ms, RARE factor = 8, number of averages = 2. Functional scans were acquired using FOV = $17 \times 9\,mm^2$, FOV saturation slice masking non-brain regions, number of slices = 21, slice thickness = 0.45, slice gap = 0.05 mm, MD = 60×30, TR = 1000 ms, TE = 11.7 ms, flip angle = 50°, volumes = 720, bandwidth = 119047 Hz. Field inhomogeneity was corrected using MAPSHIM protocol. Light stimulation was provided through a blue light laser (473 nm, LaserCentury, Shanghai Laser & Optic Century Co., Ltd; ~12–15 mW output with continuous light at the tip of the fiber) controlled by in-house software (LabVIEW, National Instruments). After an initial 50 s of rest as a baseline, 5, 10 or 20 Hz light pulses (10 ms long pulses) were applied for 10 s followed by a 50 s rest period, in a 10-block design fashion. An additional 60 s of rest were recorded after the last block of stimulation (Supplementary Figure S7a). The experimental groups (3xTgAD and wild-type mice with ChR2-mCherry) and the negative control group (wild-type mice with mCherry alone) underwent the same imaging protocol, i.e., one resting-state scan, followed by randomized 5 Hz, 10 Hz and 20 Hz evoked fMRI scans, for a total of ~40 mins of functional scan time (10 mins rest and 30 evoked). The negative control group was imaged with the same imaging protocol as the experimental groups to exclude potential heating and/or vascular photoreactivity artifacts.[34,35] Additionally, in order to exclude abnormal behavior induced by the photostimulation protocol,[36] all animals underwent the three stimulation sessions (5 Hz, 10 Hz, and 20 Hz) again while awake and freely walking in a behavior-chamber.

Analysis

Images were processed using a protocol optimized for the mouse and corrected for spikes (*3dDespike, AFNI*[37]) motion (*mcflirt, FSL* [38]) and B1 field inhomogeneity (*fast*). Automatic brain masking was carried out on the EPI using *bet*, following smoothing with a $0.3\,mm^2$ kernel (*susan*) and a 0.01 Hz high-pass filter (*fslmaths*). Nuisance regression was performed using FIX.[22] Separate classifiers were generated for rsfMRI and ofMRI. The EPIs were registered to the Allen Institute for Brain Science (AIBS) reference template ccfv3 using SyN diffeomorphic image registration (*antsIntroduction.sh, ANTS* [39])

Local connectivity was assessed with ReHo (*3dReHo*).[40,41] Pair-wise region-of-interest (ROI) analysis was carried out with respect to ROIs defined in the AIBS atlas. The ROI-averaged time series extracted with the atlas were cross-correlated to the time series from the ENTl using Pearson's correlation. The ofMRI response was examined using a general linear model (GLM) framework (*fsl_glm*). The stimulation paradigm and its first derivative were convolved using the default gamma function and used as regressors in the analysis, with motion parameters as covariates. Nomenclature and abbreviations for the brain regions are in accordance with https://atlas.brain-map.org/.

Human literature spatial meta-analysis was performed on the neuroquery.org platform, using the terms 'tauopathy' (November 8th, 2019) and 'Alzheimer's disease' (November 18th, 2021). The queries returned ~70 spatial maps depicting activation voxels in neuroimaging literature associated with each searched term, based on ~30 studies (Figure 1(a), Supplementary Figure S1).

Statistics

Imaging: Descriptive statistics for neuroimaging data are given as mean difference and [95th confidence interval] unless stated otherwise, and graphically represented as 'Gardner–Altman plots' (https://www.estimationstats.com/;[42]) If not specified, descriptive statistics are provided for left hemisphere ROIs. The statistical threshold for significance was set at $p < 0.05$, two-tailed. Voxel-wise was carried out with a non-parametric permutation-based (5000 permutations) test (*randomize*). Cluster correction was carried out with threshold-free cluster enhancement (*tfce*). Thresholded t-statistic for one-sample and two-sample t-tests ($p < 0.05$, tfce corrected) are shown as a color-coded overlay on the AIBS template. In the ofMRI dataset, the spatial response elicited in

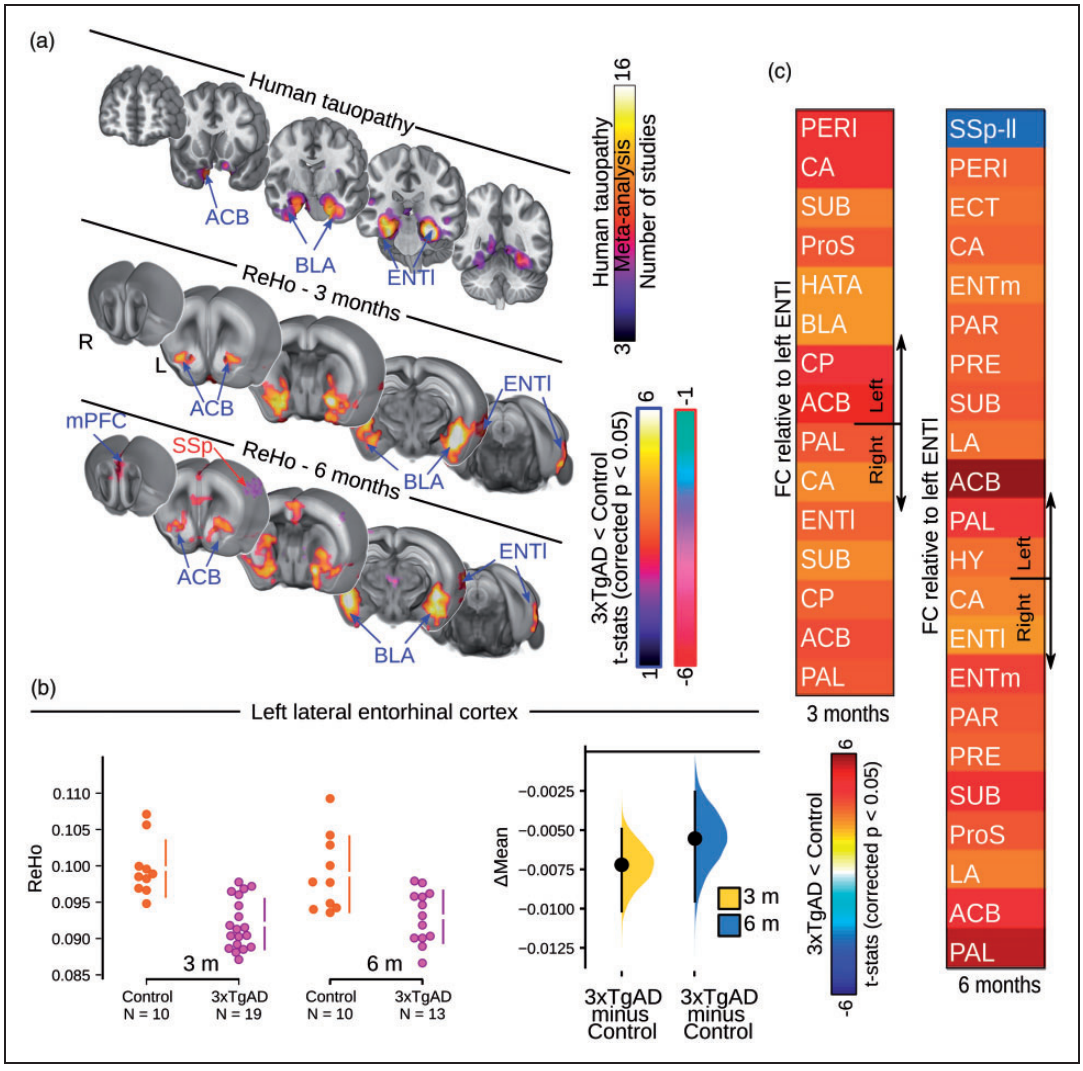

Figure 1. Loss of functional connectivity at rest in 3xTgAD overlaps with human tauopathy loci. (a) Networks implicated in human tauopathy as revealed by literature meta-analysis (top) and Regional Homogeneity (ReHo) thresholded group analysis for 3- and 6-month-old mice (middle, bottom). Significant decrease (blue arrows) in ReHo within the ENTl, ACB, and BLA in 3- and 6-month-old 3xTgAD, respectively. Significant increase in ReHo in SSp regions (red arrow). (b) ReHo distribution in the ENTl (left hemisphere: $\Delta mean_{3months} = -0.007$ [−0.010, −0.005]; $\Delta mean_{6months} = -0.006$ [−0.009, −0.003]). (c) Pair-wise ROI interactions relative to the left ENTl: decrease of functional connectivity in contralateral ENTl, ACB, BLA at both ages. Increased functional connectivity in somatosensory regions. SSp-ll: somatosensory area, lower limb; ENTl: lateral entorhinal cortex; BLA: basolateral amygdala; ACB: nucleus accumbens.

mCherry controls (without opsin, Supplementary Figure S7) was binarized, in order to obtain a visual mask (Supplementary Figure S7d, lower panel). This was then applied to the opsin-activated results after statistical comparison, in order to exclude the activation of the visual system following light stimulation, as a confounding variable.

ROI analysis was carried out with a linear mixed model using genotype and age as fixed effects and individual intercepts as random effects, using the lme4 package (1.1–21) for R (https://cran.r-project.org/, 3.5.3, "Great Truth"). Interaction effect age X genotype was also assessed, but the results revealed no interaction; this is not further reported. Significance was assessed with general linear hypothesis tests implemented in the *multcomp* (1.4–10) package and corrected with the false discovery rate. All network analyses performed were conducted voxel-wise and corrected for multiple comparisons throughout the work.

Results

Ventral networks are affected during tauopathy

To identify the networks affected in AD and tauopathy, we first performed a neuroimaging literature meta-analysis for the search terms 'Alzheimer's disease' and 'tauopathy' through the NeuroQuery library, based on loci reported in 30 studies.[30] The maps revealed by the two queries highlighted differences in their associated brain regions. The 'Alzheimer's disease' query revealed a greater involvement of the parietal, precuneus and temporal lobe regions (Supplementary Figure S1), whereas, a convergence of loci was found in ventral networks in the tauopathy query, including the entorhinal cortex, the amygdala, and the nucleus accumbens (Figure 1(a)), corresponding with areas identified in the early Braak stages.[29, 43]

To understand the physiological processes underlying network dysfunction during early AD stages, we turned to the 3xTgAD model of cerebral amyloidosis and tauopathy. To examine early pathological processes, we studied mice at a stage that we predicted would correspond to Braak ~II in humans, namely, phospho-tau in entorhinal-hippocampal-ventral areas.[29] Brain slices from 3xTgAD and control animals aged 3, 6, and 10 months were examined for immunoreactivity to 6e10 (targeting the N-terminus of beta-amyloid, Aβ, Figure 2(a) to (f)) and AT8 (targeting neurofibrillary tangle-specific phospho-tau (Ser202, Thr205) Figure 2(g) to (l)). Consistent with previous work,[23,44] no extracellular immunoreactivity was observed to 6e10 at 3 and 6 months of age (Figure 2(a) to (d)), while AT8 binding was revealed in the amygdala at 3 months (Figure 2(h)) and also observed in the hippocampus at 6 and 10 months (Figure 2(i) to (l)). However, as no immunoreactivity was detected in the ENTl area at this stage, we conclude that 3xTgAD mice aged 3–6 months represent a pre-plaque and pre-tangle stage of AD-like pathology, partially overlapping to Braak stage ~II. Therefore, the 3–6-month age range was examined for the remainder of this study as this appears similar to the early pathological state in human AD.

Functional deficits in 3xTgAD ventral network during pre-tauopathy stages

To examine spontaneous fluctuations in brain activity, we recorded longitudinally the resting state fMRI in male 3xTgAD and wild-type control mice on the same background strain (129sv/c57bl6) at 3 ($N_{3xTgAD} = 19$, $N_{controls} = 10$) and 6 months of age ($N_{3xTgAD} = 13$, $N_{controls} = 10$). The rsfMRI protocol employed here was recently compared to others in a multicenter study, which indicated elevated sensitivity and specificity for resting-state networks detected in this dataset relative to other protocols, including an awake mouse protocol.[45] One 3xTgAD mouse developed hydrocephalus, which, despite the acute condition, only marginally affected functional connectivity.[46] This animal was removed from our study following *a priori* exclusion criteria.

Firstly, we examined local connectivity coherence using the Regional Homogeneity (ReHo) method,[40] a sensitive indicator of local connectivity in mice.[41] ReHo is a data-driven approach that measures how well correlated a voxel is with its neighboring voxels, on a scale from 0 (not correlated) to 1 (completely correlated). As such, it provides an unbiased depiction of focal connectivity changes across the brain. Here, 3xTgAD mice in both age groups presented a bilateral deficit in ReHo, compared to controls, localized to the ventral-amygdaloid-striatal system (Figure 1(a)). The latter included the ENTl ($\Delta mean_{3months} = -0.007$ [–0.010, –0.005]; $\Delta mean_{6months} = -0.006$ [–0.009, –0.003], Figure 1(b)) within the retrohippocampal area, the nucleus accumbens (ACB; Supplementary Figure S2a) within the ventral striatum, basolateral amygdala (BLA; Supplementary Figure S2b) and medial prefrontal cortex (mPFC, prelimbic cortex within the mPFC reported as an example in Supplementary Figure S2c). Concurrently, 3xTgAD mice exhibited increased ReHo in somatosensory areas, such as barrel field cortex (SSp-bfd, $\Delta mean_{3months} = 0.122$ [0.005, 0.020], $\Delta mean_{6months} = 0.017$ [0.006, 0.035], Supplementary Figure S2d).

Strikingly, the functional deficit clusters, identified with the ReHo method, overlapped with homologous areas associated with tauopathy in humans, namely,

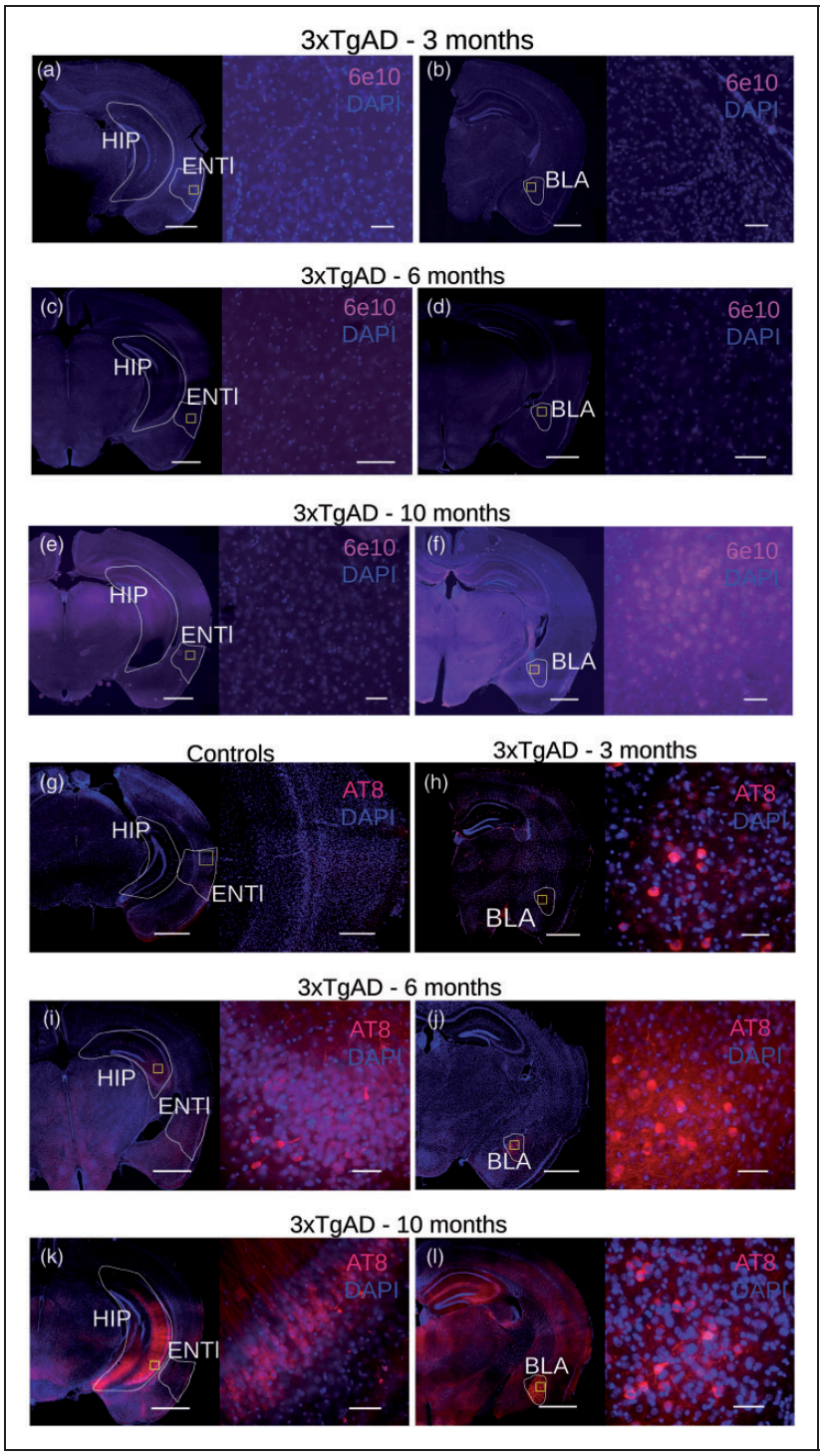

Figure 2. Immunohistochemistry for 3xTgAD characterization with 6e10-DAPI and AT8-DAPI. 3xTgAD mice show no reactivity to the N-terminus of Aβ form at both 3 and 6 months of age in the hippocampus (HIP), ENTI (a,c lower and higher magnification, left to right) and BLA (b,d, lower and higher magnification, left to right), respectively. (e) 3xTgAD mice show no reactivity to the N-terminus of Aβ form in the ENTI area at 10 months of age, lower and higher magnification, left to right. (f) Aβ-positive labeling in the BLA at 10 months, lower and higher magnification, left to right. (g) No reactivity was detected in wild-type mice (3-month-old example, lower and higher magnification, left to right), whereas 3xTgAD mice showed positive staining for phospho-tau in the amygdala area (but not for the ENTI) by 3 months of age (h, lower and higher magnification, left to right). (i) 6-month-old 3xTgAD mice show tau-positive labeling extended to the hippocampus (HIP, lower and higher magnification, left to right), whereas ENTI shows no apparent pathology; (j) tau-positive labeling is confirmed in the amygdala (BLA, lower and higher magnification, left to right). (k) 10-month-old 3xTgAD mice show tau-positive staining in the hippocampus (lower and higher magnification, left to right). ENTI, however, does not show a positive response to AT8. Confirmed tau-positive labeling was seen in the amygdala (l, lower and higher magnification, left to right). Lower magnification: 1000 μm; higher magnification: 100 μm.

the ventral-amygdaloid-striatal system. These areas represent an early target for tau aggregation, as consistently highlighted in the literature meta-analysis for the keyword 'tauopathy' through the NeuroQuery toolkit (Figure 1(a)). In contrast, no relevant overlap was found when comparing the ReHo maps with the query for "Alzheimer's disease". Thus, the 3xTgAD model, similar to other transgenic models, e.g., PSAPP, ArcAβ,[13,20,32] presents functional alterations that precede extracellular Aβ and tangle deposition and aligns better with the spatial distribution of tau pathology reported in patients. Importantly, deficits within the ventral-amygdaloid-striatal system are consistent with behavioral results in young 3xTgAD, where fear and emotional processes are highly affected.[47] Emotional control, regulated by the hippocampal-prefrontal-amygdaloid system, is also affected in pre-AD patients,[47,48] further highlighting the trans-species relevance of our results. We conclude that the pathological and functional profile in 3xTgAD, at the time points investigated here, is more consistent with a tauopathy rather than amyloid phenotype. Moreover, not all brain areas were affected in a comparable manner: the somatosensory cortex of 3xTgAD presented elevated ReHo, reminiscent of previous findings in the APP transgenic model.[49] This highlights that pathophysiology does not affect each brain region equally.

Dopamine response genes are enriched in functionally compromised regions in 3xTgAD

We hypothesized that the patterns of functional alteration were the consequence of 3xTgAD transgene products interacting with others from the brain transcriptome. To test this, we searched for gene expression patterns overlapping with the functional deficits highlighted above (Figure 1(a)). The expression profile from 4117 genes selected for their brain expression was spatially correlated with the ReHo deficits in the 3-month-old 3xTgAD dataset (Supplementary Figure S3). We compared the occurrence in biological processes in a ranked-test in the GOrilla database. Genes associated with dopamine signaling overlapped with regional deficits (Table 1, p-value$_{FDR} < 0.001$). These included genes encoding for G protein signaling (Rgs9, EntrezID = 19739, r = 0.178), G protein subunit (Gnal, EntrezID = 14680, r = 0.215), and Adenylate cyclases (Adcy5, EntrezID = 224129, r = 0.184, Adcy6, EntrezID = 11512, r = 0.142).

Changes in dopamine signaling were reported previously in an animal model of cerebral amyloidosis also overexpressing APP$_{swe}$. In addition, loss of midbrain dopamine (DA) neurons, as well as deficits in hippocampus-to-ACB signaling mediated by DA, has been observed at 3 months of age in Tg2576 mice.[50,51] In AD, alterations in DA levels or DAergic receptors are found to significantly impact synaptic plasticity and hippocampal-memory encoding.[52] Loss of DA receptors, especially D2, has been shown in areas such as the hippocampus, prefrontal cortices, and BLA [53,54] in AD patients. PET studies on AD patients also confirm a loss of striatal D2-like receptors.[55] Our results, therefore, bring supporting evidence for an interaction between the DAergic system associated with early cerebral amyloidosis and tauopathy, which leads to synaptic dysfunction.

Local functional connectivity deficits translate into whole-brain network alterations

The ENTl and associated hippocampal areas are fundamental for declarative memory encoding and retrieval.[56,57] In particular, the ENTl is among the first hubs affected in both human AD[58] and the 3xTgAD model of cerebral amyloidosis and tauopathy[23] (Figure 1(a)). As such, the ENTl was targeted for further analysis. To examine distal functional connectivity alterations at rest, we assessed pair-wise ROI interactions relative to the left-hemisphere ENTl.

Table 1. Dopamine receptor signaling pathway genes overlap with the ReHo functional deficit in 3xTgAD.

GO term	Description	p-value	FDR q-value	Enrichment
GO:0007212	Dopamine receptor signaling pathway	6.8E-9	7.62E-5	16.47
Top ranking genes				

Rgs9 – regulator of g-protein signaling 9
Adcy5 – adenylate cyclase 5
Gnal – guanine nucleotide-binding protein, alpha stimulating, olfactory type
Gnao1 – guanine nucleotide-binding protein, alpha o
Drd3 – dopamine receptor d3
Drd2 – dopamine receptor d2
Drd1a – dopamine receptor d1a
Adcy6 – adenylate cyclase 6

Functional connectivity to the ENTl was decreased in the retrohippocampal and hippocampal regions (Figure 1(c), and e.g., ENTl right hemisphere: $\Delta mean_{3months} = -0.114$ [–0.193, –0.035], $\Delta mean_{6months} = -0.127$ [–0.205, –0.058], Supplementary Figure S4a), ventral striatum (ACB, Supplementary Figure S4b), and amygdala (BLA, Supplementary Figure S4c). Similarly, an increase in functional connectivity relative to the ENTl was reported in the somatosensory cortex (lower limb, SSp-ll; Supplementary Figure S4d). These results, focusing on the ENTl-specific network, show similarities to the whole-brain functional connectivity changes assessed with ReHo, presented in an overlapped design in Supplementary Figure S5.

To confirm the connectivity results, we performed electrophysiological recordings in urethane-anesthetized 3xTgAD and control mice, *in vivo,* at 3 or 6 months of age. Field excitatory postsynaptic potentials (fEPSP) were assessed within the BLA and dentate gyrus (DG), following electrical stimulation in the ENTl (Figure 3(a) and (b)). A paired-pulse stimulation (PPS) protocol, used to assess short-term synaptic plasticity changes, was analyzed through the paired-pulse index (PPI) and revealed a quadruple effect between ROI, age, genotype, and paired-pulse intervals: $F_{(51,46)} = 28.135$, $p < 0.001$.

Specifically, no difference between 3xTgAD and controls was found for longer paired-pulse intervals in both the BLA and DG at both age points (Figure 3(a) and (b)). A strong increase in facilitation was instead reported for short intervals in both DG (e.g., 3 months old: 20 ms, z-score = –3.16, $p < 0.01$; 50 ms, z-score = –4.54, $p < 0.001$; Figure 3(a)) and BLA (e.g., 3 months old: 20 ms, z-score = –3.96,

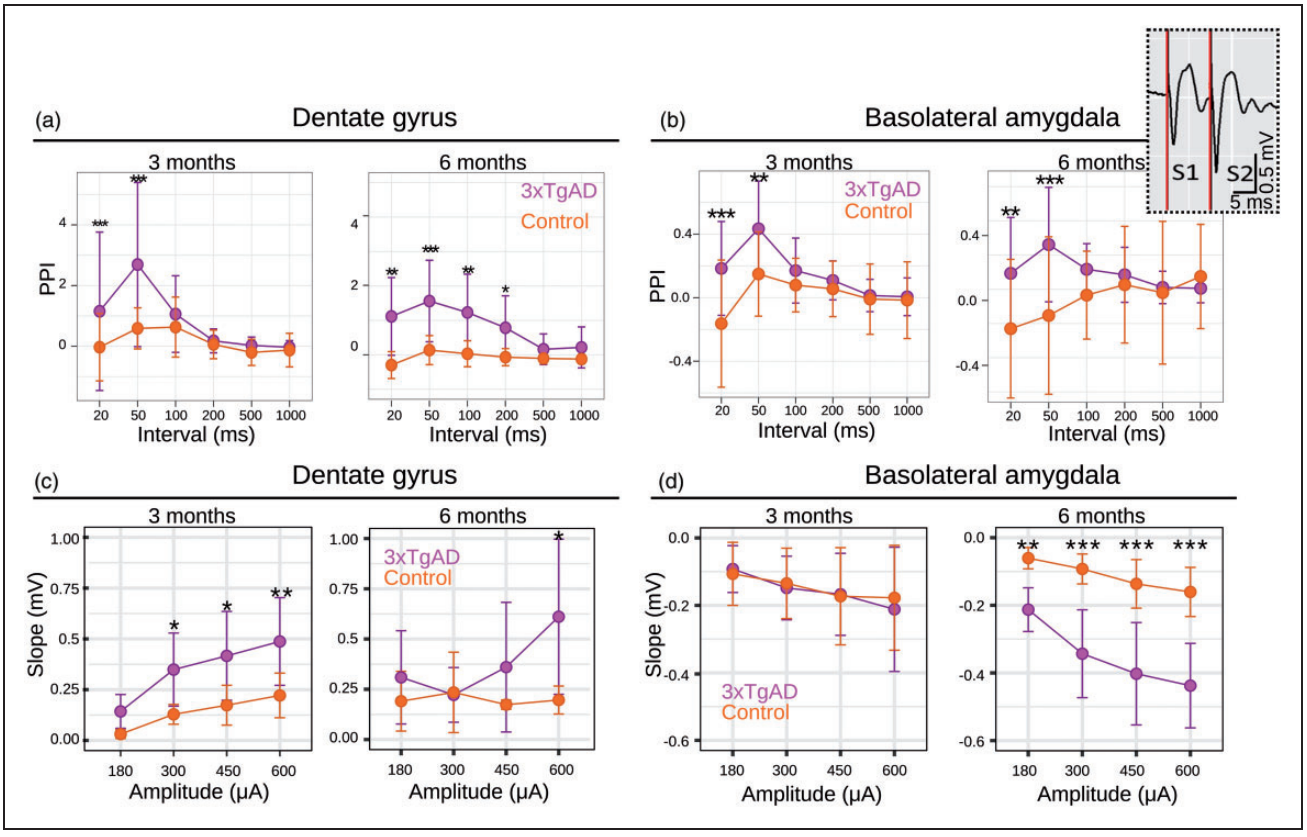

Figure 3. Paired-pulse stimulation (PPS) response measured from evoked fEPSPs in the DG (a) and BLA (b) at 3 (left panels in each section) and 6 (right panels in each section) months of age. PPS recordings in both regions show increased facilitation in 3xTgAD, at both ages. Note that controls often show paired pulse depression (negative paired-pulse index, PPI) at the same paired pulse intervals. These responses are to ENTl stimulus pairs, calculated as the PPI, at intervals within stimulus pairs of either 20, 50, 100, 200, 500 or 1000 ms. Data are plotted as mean ± SD. Input/Output curves for DG (c, 3 and 6 months left to right) and BLA (d, 3 and 6 months left to right) in response to ENTl stimulation show strengthening of synaptic connectivity in 3xTgAD. Data are plotted as mean initial fEPSP slope values ± SD. *$p < 0.05$, **$p < 0.005$, ***$p < 0.001$ (3 months old: $N_{controls} = 7$, $N_{3xTgAD} = 6$; 6 months old: $N_{controls} = 4$, $N_{3xTgAD} = 4$). Top-right inset: example of raw data from 3xTgAD mouse BLA for pulse 1 (S1) and pulse 2 (S2) at 3 months; note the increased response amplitude following pulse 2, suggesting facilitation (positive PPI) in 3xTgAD. PPS: paired-pulse stimulation; PPI: paired-pulse index; ENTl: lateral entorhinal cortex; BLA: basolateral amygdala; DG: dentate gyrus; fEPSP: field excitatory postsynaptic potential; S1–2: Stimulation (pulse) 1–2.

$p < 0.001$; 50 ms, z-score = –3.11, $p < 0.05$; Figure 3(b)); at these intervals in BLA, WT controls instead show paired-pulse depression. This overall change may indicate neuronal synaptic hyperexcitability in 3xTgAD: intracellular Ca^{2+} residuals from the first stimulus (S1) likely elicit augmented release of the presynaptic neurotransmitter in response to the second pulse (S2). This hyperexcitable neuronal profile may support the network dysfunction observed, through compensatory mechanisms in response to the compromised functional connectivity reported at rest. Additionally, the Input/Output curve (IOC) analysis for synaptic strength revealed a quadruple interaction effect between ROIs, age, genotype, and stimulation amplitude (Figure 3(c) and (d)): $F_{(35,32)} = 108.31$, $p < 0.001$. Within DG, 3xTgAD mice showed larger responses than controls by 3 months (e.g., 300 µA z-score = 2.36, $p < 0.05$ and 600 µA z-score = 2.93, $p < 0.005$; Figure 3(c), left panel). At 6 months, there was a significant difference between genotypes for the strongest current stimulus (600 µA, z-score = 2.12, $p < 0.05$), although there was a trend for increased facilitation in 3xTgAD mice compared to controls (Figure 3(c), right panel). Within the BLA, 3xTgAD mice did not show significant differences compared to controls at 3 months, whereas there was a significantly larger response at 6 months for all stimulus intensities, e.g., 300 µA ($z = –6.23$, $p < 0.001$), 450 µA ($z = –6.64$, $p < 0.001$) and 600 µA ($z = –7.1$, $p < 0.001$; Figure 3(d), right panel). Taken together, our electrophysiological *in vivo* evidence reveals hyperexcitable behavior during the evoked neuronal response in disease-relevant 3xTgAD brain regions. This suggests a dichotomous relationship between increased-evoked and reduced-spontaneous activity in AD-like vulnerable areas, where functional connectivity is highly compromised at rest.

In an exploratory analysis, we examined whole-brain network deficits in 3xTgAD mice at 3 and 6 months of age (Supplementary Figure S6a). Alterations were consistent between both age groups and localized within and between regions highlighted in the ReHo analysis, namely, in the amygdaloid/cerebral nuclei (including BLA and ACB), the ENTl and the hippocampal formation (Figure 1(a), Supplementary Figure S6). Importantly, the nodal degree distribution, i.e., the number of affected connections per ROI, was found to overlap with ReHo (Supplementary Figure S6b). This indicates that local functional connectivity deficits translate into distal functional connectivity deficits and, in turn, greater network dysfunction. Moreover, regions highlighted in the pairwise correlation analysis (amygdala and hippocampus, Supplementary Figure S2) were also found to be enriched in tau aggregates, consistent with tau dispersions across functionally connected networks.[59]

Functional connectome of the ENTl revealed by optogenetics

The ENTl was revealed above to be a major hub region affected in the 3xTgAD brain at rest. To further explore the functional consequences of this finding, we leveraged fMRI combined with optogenetics (ofMRI; Figure 4) [60] to visualize the hemodynamic response to a 10-block design photostimulation of ChR2-transfected CaMKIIα-positive (AAV5-CamKIIα-hChR2 (H134R)-mCherry) ENTl neurons ($N_{controls} = 10$, $N = 12_{3xTgAD}$; Figure 4(a) and (b), Supplementary Figure S7ab). Anatomical imaging of the optic fiber revealed that the ENTl was accurately targeted (Figure 4(c), Supplementary Figure S7c). Transfection led to robust expression at the target site (Figure 4(b), Supplementary Figure S8a). Cell bodies of transfected neurons were consistent with those of excitatory pyramidal cells (Supplementary Figure S8b). ENTl neurons faithfully responded to 5 and 20 Hz light pulse trains in both controls and 3xTgAD (Figure 4(d), Supplementary Figure S8c). Prolonged photostimulation (500 ms) applied to patched neurons *in vitro* confirmed an effective ChR2-induced inward current on both control and 3xTgAD mice *post hoc* (Supplementary Figure S8d).

There was no evidence of aberrant spontaneous behavior to photostimulation protocols in freely behaving mice, unlike seizures previously reported following photostimulation of the hippocampus in rats.[36] An unbiased voxel-wise analysis revealed the BOLD signal associated with our modeled response in controls and 3xTgAD at 3 months of age (Figure 4(e), top and middle rows respectively) in several regions, including the hippocampal formation (hippocampus and retro hippocampal areas), the amygdaloid area (e.g., BLA), the ventral striatum (ACB), the prefrontal and the insular areas. Similar results were reported for the 6-month age point (Supplementary Figure S9, left and middle panels). Optogenetically-evoked activity was predominantly confined to the ipsilateral hemisphere, despite the presence of contralateral projections, as predicted by viral tracers (Figure 4(e) bottom row, spatial correlation $r = 0.36$). Interestingly, the application of the hidden-Markov model onto the same data in another study [61] reveals a more complex optogenetically-elicited response, where a delayed contralateral activation is also reported. This supports the notion of a nuanced response as a function of stimulation frequency and post-stimulation intervals. The response elicited through photostimulation of the ENTl was comparable between mice at 3 and 6 months of age, indicating a stable expression allowing for longitudinal analysis. A negative control carried out in healthy wild-type mice ($N_{mCherry\text{-}controls} = 9$) transfected with mCherry alone (Figure 4(b)) did not reveal the presence of a

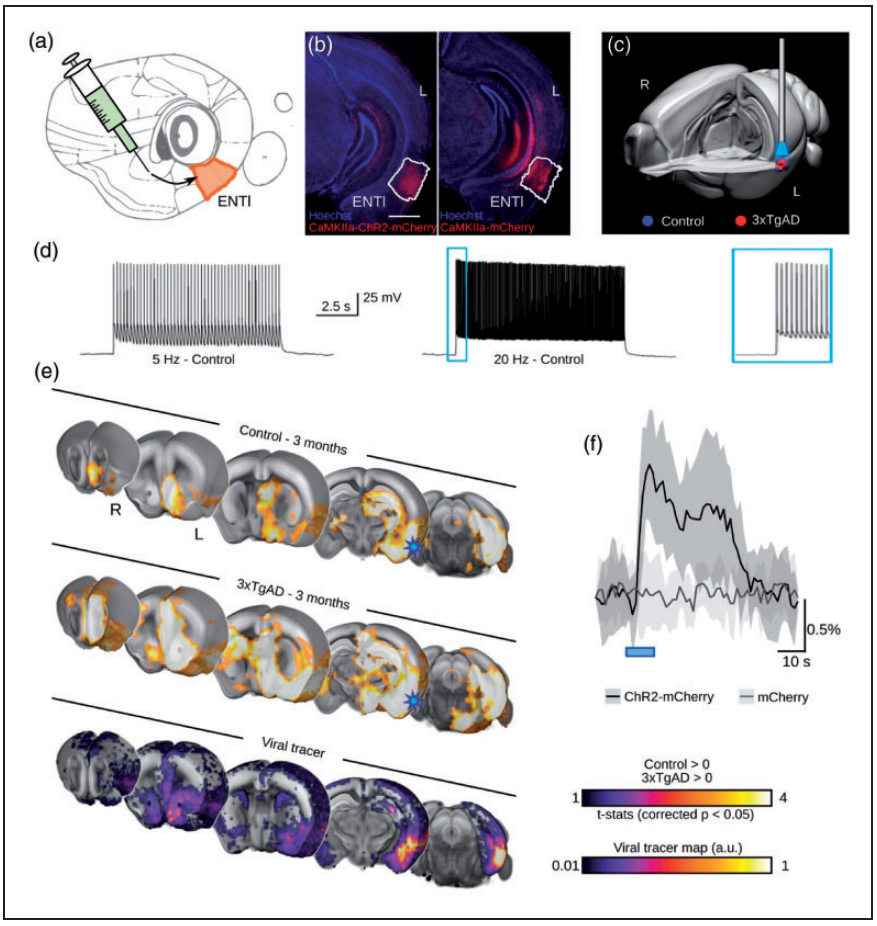

Figure 4. Optogenetic modulation of the lateral entorhinal cortex. (a) Diagram of stereotaxic injection in the left ENTl (in mm from Bregma and middle line: AP: –2.8, ML: +4.2, DV: –2.6). (b) ChR2-mCherry/Hoechst (left) and mCherry/Hoechst (right) indicate successful targeting of the ENTl and stable transfection. (c) 3-d rendering of fiber tip position for each experimental animal, red dots indicate 3xTgAD subjects (N = 12) and blue dots indicate controls (N = 10). (d) Optogenetic stimulation of ChR2-transfected neurons at 5 Hz and 20 Hz *in vitro* shows frequency-locked spiking activity. (e) Optogenetically-locked BOLD response overlaps with density projection maps. Top and middle sections indicating one-sample t-test for stimulation-locked BOLD response in the control group and 3xTgAD mice (N = 10, N = 12, respectively; $p < 0.05$ corrected) highlighting activation in key regions related to ENTl projections, i.e., HIP, BLA, ACB and mPFC; AIBS tracer projection density map with injection in ENTl (experiment ID: #114472145; bottom section). Stimulation site (ENTl) indicated with a blue star. (f) BOLD response profile, averaged across 10 blocks, following 20 Hz stimulation in control mice injected with ChR2-mCherry (N = 10) and control mice injected with mCherry only (N = 9) shows an opsin-dependent BOLD response. AP: anterior-posterior; ML: medio-lateral; DV: dorso-ventral; HIP: hippocampus; BLA: basolateral amygdala; ACB: nucleus accumbens; mPFC: medial prefrontal cortex. Scale bar: 1000 μm

stimulation-induced response, except for a visual-associated response of the lateral geniculate nucleus and superior colliculus, probably due to the fiber illumination received as a direct visual response to retinal illumination (Supplementary Figure S7d). Hence, we concluded that the response recorded with ofMRI was not associated with potential heating and/or vascular photoreactivity artifacts. Photostimulation at frequencies ranging from 5 to 20 Hz indicated spatially overlapping results (Supplementary Figure S7e), in contrast to previous research.[62] In fact, the non-specific, visually-associated response amplitude was stronger at lower frequencies (Supplementary Figure S7d, upper panel), while the opsin-associated response was more marked at 20 Hz (Figure 4(e), Supplementary Figure S9). The areas associated with a visual response elicited with 5 Hz stimulation were subsequently binarized and masked out from our results and the remainder of the analysis focused on the 20 Hz paradigm (Supplementary Figure S7d, lower panel).

Potentiated hemodynamic response and neuronal activity in 3xTgAD

To assess response differences across the brain, a non-parametric second-level analysis comparing the

amplitude of activation between 3xTgAD and controls was carried out (Figure 5, central segment). Group size at 6 months of age was reduced due to group attrition, e.g., detachment of the implant. Therefore, group sizes differed between 3 months ($N_{controls} = 10$, $N_{3xTgAD} = 12$) and 6 months ($N_{controls} = 8$, $N_{3xTgAD} = 10$) of age. Surprisingly, and in contrast to the results observed at rest, 3xTgAD mice showed significantly larger responses across several regions compared to controls at 3 months. The regions affected included the ipsilateral dorsal hippocampus, ACB, mPFC, cingulate and retrosplenial areas, and contralateral ENTl. The presence of an effect at 6 months could not be detected, potentially due to the reduced group size, or to a normalization of the response at a later age.

To examine local response amplitude, contrast of parameter estimates (COPEs) were extracted from ROIs highlighted in the voxel-wise comparison: ENTl ($\Delta mean_{3months} = 0.044$, [0.022, 0.070]), ACB ($\Delta mean_{3months} = 0.15$ [0.0106, 0.298]), mPFC (Figure 5(c), $\Delta mean_{3months} = 0.283$ [0.161, 0.431]) and DG (Figure 5(f)). Similar results were present at lower stimulation frequencies, although the more distal regions had a mitigated effect at lower frequencies (example for 10 Hz, ENTl: $\Delta mean_{3months} = 0.008$, [–0.08, 0.09]). Data acquired at rest, prior to optogenetic stimulation, indicated ReHo deficits converging with that acquired in the previous dataset, replicating our observations above, despite lower acquisition quality due to a room temperature receiver coil instead of a cryoprobe coil (Supplementary Figure S10).

To confirm the increased response observed in ofMRI, we examined neuronal excitability *ex vivo* in two projection areas highlighted above: the DG, within the hippocampus, and the infralimbic area (ILA), within mPFC. Acute brain slice electrophysiology indicated that excitatory neurons of 3xTgAD, in both ILA (Figure 5(a) and (b)) and DG

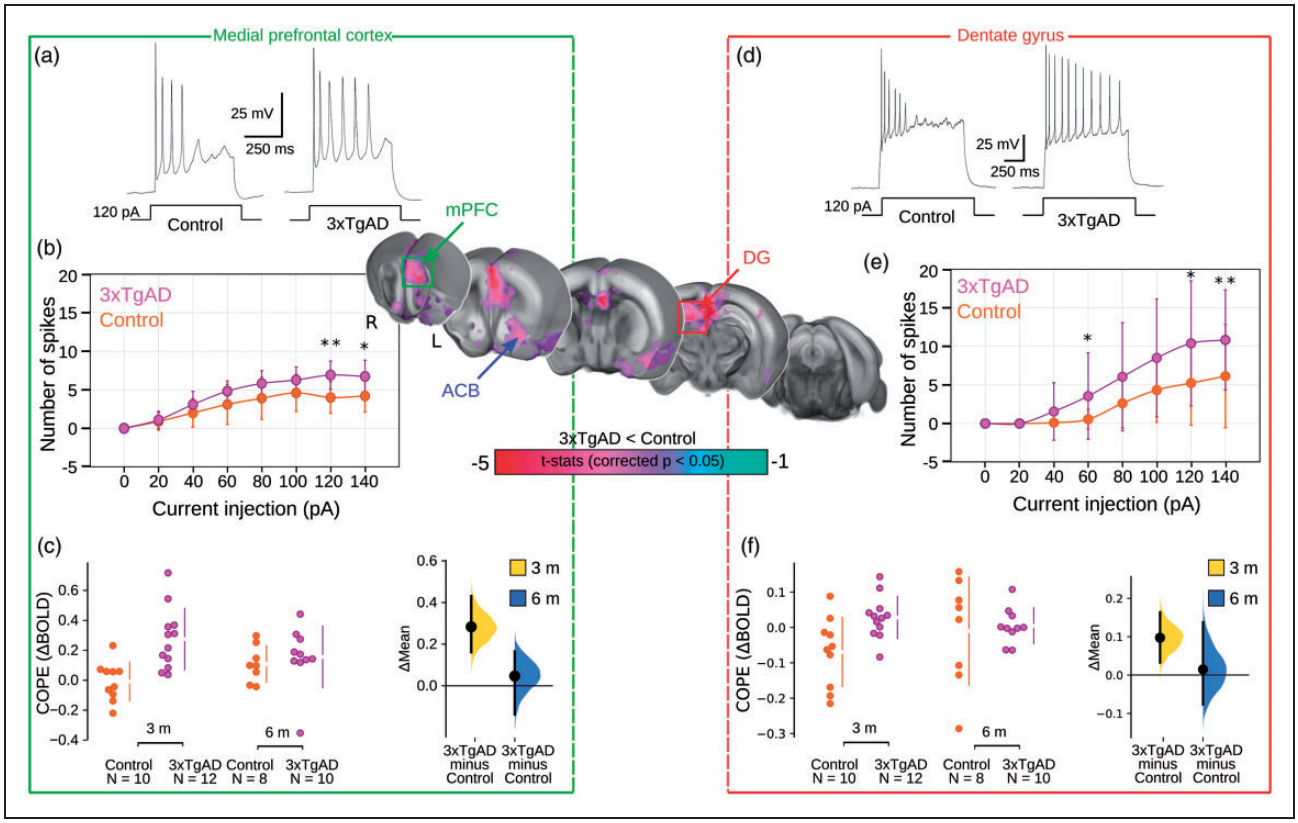

Figure 5. Increased optogenetically-locked response in 3xTgAD compared to controls at 3 months. Central panel: Two-sample t-test showing significantly higher response ($p < 0.05$, corrected) in 3xTgAD compared to controls in AD-like vulnerable regions, such as mPFC and DG. Results arising from the mPFC are included in the green rectangle (a,b,c) and results from DG are in the red rectangle (d,e,f). Representative action potential firing patterns to 120 pA injection in ILA (within mPFC) pyramidal cells ($N_{controls} = 4$, $n = 10$/$N_{3xTgAD} = 4$, $n = 11$) and DG granule cells ($N_{controls} = 4$, $n = 29$/$N_{3xTgAD} = 5$, $n = 18$) respectively (a,d). The evoked spike number during various injected currents in ILA pyramidal cells and DG granule cells, respectively (b,e). The data are plotted as mean action potential numbers ± 1 SD. The statistical significance is presented with asterisks (*$p < 0.05$, **$p < 0.01$ by Mann-Whitney U test). COPEs are represented for 3xTgAD and controls at both age points for mPFC and DG, respectively (c, f). mPFC: medial prefrontal cortex; DG: dentate gyrus; COPE: contrast of parameter estimates; ACB: nucleus accumbens; ILA: infralimbic cortex.

(Figure 5(e) and (d)), were prone to increase the number of spikes derived by current injection compared to controls, but ILA neurons showed enhancement of afterhyperpolarization (AHP) latency and half-width of the action potential, a phenotype consistent with previous results [63] (Supplementary Table S2), while spike morphology was comparatively unaltered (Supplementary Table S3). To examine how the alterations of the ENTl functional projectome at 3 months related to a loss of functional connectivity at rest, we projected the two responses onto the same template (Supplementary Figure S9, right panel). We found that several of the ROIs, presenting decreased functional connectivity at rest, were responding with greater amplitude to optogenetically-driven neuronal activity. This was the case for regions encompassing the ventral striatum (ACB), the dorsal DG within the hippocampal formation and prefrontal regions.

In sum, 3xTgAD mice showed decreased functional connectivity at rest and, in contrast, an increased response during optogenetic stimulation. Direct neuronal recordings, both *in vivo* and *ex vivo*, showed a hyperactive phenotype. Taken together, these results support a hypo-connected/hyper-responsive dichotomy characterizing rest vs. evoked states in early stages of pathology progression in 3xTgAD.

Discussion

Neurological disorders, including tauopathies such as AD, are one of the greatest challenges for modern medicine. The absence of disease-modifying treatment for AD represents a major loss for the millions of patients affected worldwide. A detailed understanding of AD mechanisms across both spatial and temporal scales would provide a translational opportunity to facilitate the drug development process.

The triple mutation genotype of the 3xTg mouse model for AD leads to manifestation of AD-like beta-amyloid plaques and neurofibrillary tangles later in life.[23] At the early-pathological states investigated here (3 and 6 months of age), however, this mouse model shows no tangles or plaques, although there is clear phospho-tau accumulation by 3 months of age, together with long-range connectivity deficits. These functional connectivity deficits cluster in tau-vulnerable regions (ventral regions) already by 3 months, and overlap with areas affected by tauopathy in humans, resulting in a phenotype that can be attributed to tauopathy. This underpins the notion of a tight coupling between functional connectivity and tau progression,[59] supported by molecular work.[64] Further, a study comparing 3xTgAD with a mouse model for sporadic-AD shows a degree of overlap between the two.[65] As such, the evidence presented here suggests that 3xTgAD mice, at the ages investigated, may express characteristics that resemble the phenotype of sporadic-AD, where toxic tau deposition appears prior to beta-amyloid accumulation.[9] Overall, these observations support evidence for a tau-seeding hypothesis as the primary pathological driver in the early stages of life in 3xTgAD.[29, 66]

Importantly, our results are also compatible with modern hypotheses for the amyloid cascade. Buckner and colleagues demonstrated that network dysfunction overlapped and preceded amyloid deposition in AD subjects, revealed by PET.[67] Bero and colleagues demonstrated in APP transgenic mouse models that patterns of hyper-connectivity at a young age correlated with amyloid plaque distribution later in life.[49] Our results support the notion that local and distal network dysfunction at rest impairs information transmission and processing. This leads to increased metabolic demand during evoked activity, which putatively leads to circuit exhaustion and further accumulation of Aβ species through increased neuronal activity.[68] It will be important to confirm this model prediction in older 3xTgAD mice.

A key finding in the present work is that markedly weaker resting connectivity patterns were paired with an increased response to either optogenetically- or electrically-driven neuronal activity. How might this 'rest:decrease/evoked:increased' dichotomy in brain activity co-exist with an increase in neuronal excitability following stimulation and increased metabolic demands (Figure 5, Supplementary Figure S9 right panel)? A potential mechanism is supported by *in vivo* electrophysiological recordings in the areas affected by tau accumulation (BLA, hippocampus); thus, neuronal hyperexcitability in 3xTgAD may result in these two states coexisting due to: i) less 'organized' neuronal activity, which may underlie the reduced functional connectivity correlation strength within and across clusters at rest, and ii) increased neural response to synaptic activation, as also reported with ofMRI.

The dichotomy of the direction of these changes in resting and evoked activity, specifically within the ENTl network, mirrors several findings in preclinical and early stages of AD patients, and further supports a primary involvement of the ENTl areas in the beginning of tau seeding activity in early AD.[69] On one hand, decreased functional connectivity is found in mild AD patients at rest, in areas related to the default-mode network, including the hippocampal formation.[70] On the other hand, task-based fMRI studies show increased activity in memory-related areas in subjects at risk of AD but who are cognitively still normal (e.g., APOEε4 carriers), suggesting a dichotomy in network organization of the brain at rest and in engaged status.[71] Taken together, our findings help to reconcile

apparent discordant results put forward in early AD subjects.[15, 17, 31] The seeding hypothesis can be further connected to other models of axonal degeneration and inflammation [6] and, thus, provides a coherent description of the pathophysiology taking place in early AD.

Importantly, no single study is ever perfect and there are important limitations and areas for further investigation from the present work. Here, we only used male 3xTgAD at 3 and 6 months of age, and this limits the extension of our interpretation to both sexes, particularly given the high prevalence of female cases of AD. In addition, it is important to further assess our described dichotomy between rest/activated states with optogenetic stimulation of targets that show *increased* signal at rest, such as the somatosensory areas reported in Figure 1(a) and (c). Lastly, the different anesthesia regimes between the electrophysiological recordings and the neuroimaging side of the work represent a potential confound, albeit research previously conducted supports comparable effects of Urethane and Med/Iso regimens on rsfMRI functional connectivity.[33]

Conclusions

The work presented here provides important insight into how the seemingly discordant prior reports of either increased or decreased brain activity/connectivity in AD patients can co-exist within the same AD-like pathological state. The functional deficits found in the present study, within and relative to the temporal and ventral brain areas in 3xTgAD mice, recapitulate several important effects described in pre-AD subjects with functional neuroimaging. Importantly, we postulate a disruption in DAergic signaling pathways as one of the earliest features characterizing AD development. Moreover, photo/electrical stimulation of the ENTl leads to a marked increase in BOLD/synaptic responses in several core projection areas of the AD brain. The dichotomic behavior between resting and evoked functional responses, taking place during the early stages of cerebral amyloidosis and tauopathy, reveals an endophenotype in line with the human tauopathy profile. This suggests that similar pathophysiological mechanisms might be the cause of network dysfunction in clinical cases, providing an understanding of the underlying mechanisms leading to functional deficits preceding this neurodegenerative disorder.

Funding

The author(s) disclosed receipt of the following financial support for the research, authorship, and/or publication of this article: This work was supported by SBIC core funding, SBIC award #2017 to FM and #2016 to JGr. FM was supported by a Ph.D. scholarship funded through the ARAP scholarship and the University of Manchester (awarded to JGi). This work was also supported by the A*STAR Investigatorship (awarded to YF) and JCO grant (BMSI/15-800003-SBIC-OOE) awarded to SJ. This work was also supported by the A*STAR Investigatorship (awarded to YF) and JCO grant (BMSI/15-800003-SBIC-OOE) awarded to SJ.

Acknowledgements

All procedures conducted in the UK were performed in accordance with the UK Animals (Scientific Procedures) Act 1986 and the University of Manchester Ethical Review Panel under Home Office license PPL 70/7843. All experiments performed in Singapore Bioimaging Consortium, A*STAR, Singapore, were in accordance with the ethical standards of the Institutional Animal Care and Use Committee (A*STAR Biological Resource Centre, Singapore, IACUC #171203). The rsfMRI and ofMRI datasets supporting the conclusions of this article are available on a CCO license in the OpenNeuro repository, https://openneuro.org/ (DOI: 10.18112/openneuro.ds001890.v1.0.1, 10.18112/openneuro.ds002134.v1.0.0).

Declaration of conflicting interests

The author(s) declared no potential conflicts of interest with respect to the research, authorship, and/or publication of this article.

Authors' contributions

FM: Conceptualization, Formal analysis, Investigation, Methodology, Validation, Visualization, Writing – original draft, Writing – review and editing, Funding acquisition.
LYY, RB, LS, HGB, SHB, CYL, HM, CLT, JHL: Validation, Writing – Review & Editing
RB: Software, Methodology, Writing – Review & editing.
CH: Writing – reviewing and editing, Analysis interpretation
YF, SJ, MKPL: Validation, Resources, Writing – Review & Editing, Funding acquisition.
MO: Resources, Writing – Review & Editing, Supervision, Funding acquisition.
JGi: Conceptualization, Resources, Writing – Review & Editing, Supervision, Funding acquisition.
JGr: Conceptualization, Methodology, Formal analysis, Data curation, Software, Resources, Writing – Review & Editing, Supervision, Funding acquisition.

ORCID iDs

Francesca Mandino https://orcid.org/0000-0002-5605-0854
Renzhe Bi https://orcid.org/0000-0001-7173-064X

Supplemental material

Supplemental material for this article is available online.

References

1. Ballatore C, Lee VM-Y and Trojanowski JQ. Tau-mediated neurodegeneration in Alzheimer's disease and related disorders. *Nat Rev Neurosci* 2007; 8: 663–672.

2. Hardy J and Selkoe DJ. The amyloid hypothesis of Alzheimer's disease: progress and problems on the road to therapeutics. *Science* 2002; 297: 353–356.
3. Bali J, Gheinani AH, Zurbriggen S, et al. Role of genes linked to sporadic Alzheimer's disease risk in the production of β-amyloid peptides. *Proc Natl Acad Sci U S A* 2012; 109: 15307–15311.
4. Morris GP, Clark IA and Vissel B. Questions concerning the role of amyloid-β in the definition, aetiology and diagnosis of Alzheimer's disease. *Acta Neuropathol* 2018; 136: 663–689.
5. Krstic D and Knuesel I. The airbag problem – a potential culprit for bench-to-bedside translational efforts: relevance for Alzheimer's disease. *Acta Neuropathol Commun* 2013; 1: 62.
6. Krstic D and Knuesel I. Deciphering the mechanism underlying late-onset Alzheimer disease. *Nat Rev Neurol* 2013; 9: 25–34.
7. Huang L-K, Chao S-P and Hu C-J. Clinical trials of new drugs for Alzheimer disease. *J Biomed Sci* 2020; 27: 18.
8. Aisen PS, Vellas B and Hampel H. Moving towards early clinical trials for amyloid-targeted therapy in Alzheimer's disease. *Nat Rev Drug Discov* 2013; 12: 324.
9. Arnsten AFT, Datta D, Del Tredici K, et al. Hypothesis: Tau pathology is an initiating factor in sporadic Alzheimer's disease. *Alzheimers Dement* 2021; 17: 115–124.
10. Braak H, D and Tredici K. Alzheimer-associated pathology in the extracellular space. *Adv Anat Embryol Cell Biol* 2015; 215: 75–93.
11. Braak H, Thal DR, Ghebremedhin E, et al. Stages of the pathologic process in Alzheimer disease: age categories from 1 to 100 years. *J Neuropathol Exp Neurol* 2011; 70: 960–969.
12. Sheline YI, Morris JC, Snyder AZ, et al. APOE4 allele disrupts resting state fMRI connectivity in the absence of amyloid plaques or decreased CSF Aβ42. *J Neurosci* 2010; 30: 17035–17040.
13. Shah D, Praet J, Latif Hernandez A, et al. Early pathologic amyloid induces hypersynchrony of BOLD resting-state networks in transgenic mice and provides an early therapeutic window before amyloid plaque deposition. *Alzheimers Dement* 2016; 12: 964–976.
14. Sperling RA, Aisen PS, Beckett LA, et al. Toward defining the preclinical stages of Alzheimer's disease: recommendations from the National Institute on Aging-Alzheimer's association workgroups on diagnostic guidelines for Alzheimer's disease. *Alzheimers Dement* 2011; 7: 280–292.
15. Filippini N, MacIntosh BJ, Hough MG, et al. Distinct patterns of brain activity in young carriers of the APOE-4 allele. *PNAS* 2009; 106: 7209–7214.
16. Kobeleva X, Firbank M, Peraza L, et al. Divergent functional connectivity during attentional processing in Lewy body dementia and Alzheimer's disease. *Cortex* 2017; 92: 8–18.
17. Braskie MN, Medina LD, Rodriguez-Agudelo Y, et al. Increased fMRI signal with age in familial Alzheimer's disease mutation carriers. *Neurobiol Aging* 2012; 33: 424. e11–424.e21.
18. Palmqvist S, Schöll M, Strandberg O, et al. Earliest accumulation of β-amyloid occurs within the default-mode network and concurrently affects brain connectivity. *Nat Commun* 2017; 8: 1214.
19. Padmanabhan P, Kneynsberg A and Götz J. Super-resolution microscopy: a closer look at synaptic dysfunction in Alzheimer disease. *Nat. Rev. Neurosci* 2021; 12: 723–740.
20. Shah D, Jonckers E, Praet J, et al. Resting state fMRI reveals diminished functional connectivity in a mouse model of amyloidosis. *PLoS ONE* 2013; 8: e84241.
21. Grandjean J, Schroeter A, He P, et al. Early alterations in functional connectivity and white matter structure in a transgenic mouse model of cerebral amyloidosis. *J Neurosci* 2014; 34: 13780–13789.
22. Zerbi V, Grandjean J, Rudin M, et al. Mapping the mouse brain with rs-fMRI: an optimized pipeline for functional network identification. *Neuroimage* 2015; 123: 11–21.
23. Oddo S, Caccamo A, Shepherd JD, et al. Triple-transgenic model of Alzheimer's disease with plaques and tangles: intracellular abeta and synaptic dysfunction. *Neuron* 2003; 39: 409–421.
24. Mastrangelo MA and Bowers WJ. Detailed immunohistochemical characterization of temporal and spatial progression of Alzheimer's disease-related pathologies in male triple-transgenic mice. *BMC Neurosci* 2008; 9: 81.
25. Yeh C-Y, Vadhwana B, Verkhratsky A, et al. Early astrocytic atrophy in the entorhinal cortex of a triple transgenic animal model of Alzheimer's disease. *ASN Neuro* 2011; 3: 271–279.
26. Zuo M, Xu Y, Zhang X, et al. Aberrant brain regional homogeneity and functional connectivity of entorhinal cortex in vascular mild cognitive impairment: a resting-state functional MRI study. *Front Neurol* 2019; 9: 1177.
27. Zhou M, Zhang F, Zhao L, et al. Entorhinal cortex: a good biomarker of mild cognitive impairment and mild Alzheimer's disease. *Rev Neurosci* 2016; 27: 185–195.
28. Khan UA, Liu L, Provenzano FA, et al. Molecular drivers and cortical spread of lateral entorhinal cortex dysfunction in preclinical Alzheimer's disease. *Nat Neurosci* 2014; 17: 304–311.
29. Furman JL, Vaquer-Alicea J, White CL, 3rd, et al. Widespread tau seeding activity at early braak stages. *Acta Neuropathol* 2017; 133: 91–100.
30. Dockès J, Poldrack RA, Primet R, et al. NeuroQuery, comprehensive meta-analysis of human brain mapping. *Elife* 2020; 9. doi: 10.7554/eLife.53385.
31. Sheline YI, Raichle ME, Snyder AZ, et al. Amyloid plaques disrupt resting state default mode network connectivity in cognitively normal elderly. *Biol Psychiatry* 2010; 67: 584–587.
32. Grandjean J, Derungs R, Kulic L, et al. Complex interplay between brain function and structure during cerebral amyloidosis in APP transgenic mouse strains revealed by multi-parametric MRI comparison. *Neuroimage* 2016; 134: 1–11.
33. Grandjean J, Schroeter A, Batata I, et al. Optimization of anesthesia protocol for resting-state fMRI in mice based

on differential effects of anesthetics on functional connectivity patterns. *Neuroimage* 2014; 102 Pt 2: 838–847.
34. Christie IN, Wells JA, Southern P, et al. fMRI response to blue light delivery in the naïve brain: implications for combined optogenetic fMRI studies. *Neuroimage* 2013; 66: 634–641.
35. Rungta RL, Osmanski B-F, Boido D, et al. Light controls cerebral blood flow in naive animals. *Nat Commun* 2017; 8: 14191.
36. Weitz AJ, Fang Z, Lee HJ, et al. Optogenetic fMRI reveals distinct, frequency-dependent networks recruited by dorsal and intermediate hippocampus stimulations. *Neuroimage* 2015; 107: 229–241.
37. Cox RW. AFNI: software for analysis and visualization of functional magnetic resonance neuroimages. *Comput Biomed Res* 1996; 29: 162–173.
38. Smith SM, Jenkinson M, Woolrich MW, et al. Advances in functional and structural MR image analysis and implementation as FSL. *Neuroimage* 2004; 23: S208–S219.
39. Avants BB, Tustison N and Song G. Advanced normalization tools (ANTS). *Insight J* 2009; 2: 1–35.
40. Zang Y, Jiang T, Lu Y, et al. Regional homogeneity approach to fMRI data analysis. *Neuroimage* 2004; 22: 394–400.
41. Wu T, Grandjean J, Bosshard SC, et al. Altered regional connectivity reflecting effects of different anaesthesia protocols in the mouse brain. *Neuroimage* 2017; 149: 190–199.
42. Ho J, Tumkaya T, Aryal S, et al. Moving beyond P values: data analysis with estimation graphics. *Nat Methods* 2019; 16: 565–566.
43. Braak H and Braak E. Neuropathological stageing of Alzheimer-related changes. *Acta Neuropathol* 1991; 82: 239–259.
44. Davis KE, Fox S and Gigg J. Increased hippocampal excitability in the 3xTgAD mouse model for Alzheimer's disease in vivo. *PLoS One* 2014; 9: e91203.
45. Grandjean J, Canella C, Anckaerts C, et al. Common functional networks in the mouse brain revealed by multi-centre resting-state fMRI analysis. *Neuroimage* 2020; 205: 116278.
46. Mandino F, Yeow LY, Gigg J, et al. Preserved functional networks in a hydrocephalic mouse. *Matters* 2019; 5: e201905000001.
47. España J, Giménez-Llort L, Valero J, et al. Intraneuronal β-Amyloid accumulation in the amygdala enhances fear and anxiety in Alzheimer's disease transgenic mice. *Biol Psychiatry* 2010; 67: 513–521.
48. Sturm VE, Yokoyama JS, Seeley WW, et al. Heightened emotional contagion in mild cognitive impairment and Alzheimer's disease is associated with temporal lobe degeneration. *Proc Natl Acad Sci U S A* 2013; 110: 9944–9949.
49. Bero AW, Bauer AQ, Stewart FR, et al. Bidirectional relationship between functional connectivity and amyloid-β deposition in mouse brain. *J Neurosci* 2012; 32: 4334–4340.
50. Cordella A, Krashia P, Nobili A, et al. Dopamine loss alters the hippocampus-nucleus accumbens synaptic transmission in the Tg2576 mouse model of Alzheimer's disease. *Neurobiol Dis* 2018; 116: 142–154.
51. Nobili A, Latagliata EC, Viscomi MT, et al. Dopamine neuronal loss contributes to memory and reward dysfunction in a model of Alzheimer's disease. *Nat. Commun* 2017; 8: 1–14.
52. Koch G, Esposito Z, Codecà C, et al. Altered dopamine modulation of LTD-like plasticity in Alzheimer's disease patients. *Clin Neurophysiol* 2011; 122: 703–707.
53. Joyce JN, Kaeger C, Ryoo H, et al. Dopamine D2 receptors in the hippocampus and amygdala in Alzheimer's disease. *Neurosci Lett* 1993; 154: 171–174.
54. Kemppainen N, Laine M, Laakso MP, et al. Hippocampal dopamine D2 receptors correlate with memory functions in Alzheimer's disease. *Eur J Neurosci* 2003; 18: 149–154.
55. Tanaka Y, Meguro K, Yamaguchi S, et al. Decreased striatal D2 receptor density associated with severe behavioral abnormality in Alzheimer's disease. *Ann Nucl Med* 2003; 17: 567–573.
56. van Strien NM, Cappaert NLM and Witter MP. The anatomy of memory: an interactive overview of the parahippocampal–hippocampal network. *Nat Rev Neurosci* 2009; 10: 272–282.
57. Buzsáki G and Moser EI. Memory, navigation and theta rhythm in the hippocampal-entorhinal system. *Nat Neurosci* 2013; 16: 130–138.
58. Van Hoesen GW, Hyman BT and Damasio AR. Entorhinal cortex pathology in Alzheimer's disease. *Hippocampus* 1991; 1: 1–8.
59. Franzmeier N, Rubinski A, Neitzel J, et al. Functional connectivity associated with tau levels in ageing, Alzheimer's, and small vessel disease. *Brain* 2019; 142: 1093–1107.
60. Lee JH, Durand R, Gradinaru V, et al. Global and local fMRI signals driven by neurons defined optogenetically by type and wiring. *Nature* 2010; 465: 788–792.
61. Salvan P, Lazari A, Vidaurre D, et al. Frequency modulation of entorhinal cortex neuronal activity drives distinct frequency-dependent states of brain-wide dynamics. *Cell Rep* 2021; 37: 109954.
62. Chan RW, Leong ATL, Ho LC, et al. Low-frequency hippocampal–cortical activity drives brain-wide resting-state functional MRI connectivity. *Proc Natl Acad Sci U S A* 2017; 114: E6972–E6981.
63. Wang L, Kang H, Li Y, et al. Cognitive recovery by chronic activation of the large-conductance calcium-activated potassium channel in a mouse model of Alzheimer's disease. *Neuropharmacology* 2015; 92: 8–15.
64. Clavaguera F, Akatsu H, Fraser G, et al. Brain homogenates from human tauopathies induce tau inclusions in mouse brain. *Proc Natl Acad Sci U S A* 2013; 110: 9535–9540.
65. Chen Y, Liang Z, Blanchard J, et al. A non-transgenic mouse model (icv-STZ mouse) of Alzheimer's disease: Similarities to and differences from the transgenic model (3xTg-AD mouse). *Mol Neurobiol* 2013; 47: 711–725.

66. Holmes BB, Furman JL, Mahan TE, et al. Proteopathic tau seeding predicts tauopathy in vivo. *Proc Natl Acad Sci U S A* 2014; 111: E4376–E4385.
67. Buckner RL, Snyder AZ, Shannon BJ, et al. Molecular, structural, and functional characterization of Alzheimer's disease: evidence for a relationship between default activity, amyloid, and memory. *J Neurosci* 2005; 25: 7709–7717.
68. Bero AW, Yan P, Roh JH, et al. Neuronal activity regulates the regional vulnerability to amyloid-β deposition. *Nat Neurosci* 2011; 14: 750–756.
69. Kaufman SK, Del Tredici K, Thomas TL, et al. Tau seeding activity begins in the transentorhinal/entorhinal regions and anticipates phospho-tau pathology in Alzheimer's disease and PART. *Acta Neuropathol* 2018; 136: 57–67.
70. Greicius MD, Srivastava G, Reiss AL, et al. Default-mode network activity distinguishes Alzheimer's disease from healthy aging: evidence from functional MRI. *Proc Natl Acad Sci U S A* 2004; 101: 4637–4642.
71. Bookheimer SY, Strojwas MH, Cohen MS, et al. Patterns of brain activation in people at risk for Alzheimer's disease. *N Engl J Med* 2000; 343: 450–456.